JACS
JOURNAL OF THE AMERICAN CHEMICAL SOCIETY

Article

pubs.acs.org/JACS

Super-Resolution Mapping of Photogenerated Electron and Hole Separation in Single Metal−Semiconductor Nanocatalysts

Ji Won Ha, T. Purnima A. Ruberu, Rui Han, Bin Dong, Javier Vela,* and Ning Fang*

Ames Laboratory, U.S. Department of Energy, and Department of Chemistry, Iowa State University, Ames, Iowa 50011, United States

Supporting Information

ABSTRACT: Metal−semiconductor heterostructures are promising visible light photocatalysts for many chemical reactions. Here, we use high-resolution superlocalization imaging to reveal the nature and photocatalytic properties of the surface reactive sites on single Au−CdS hybrid nanocatalysts. We experimentally reveal two distinct, incident energy-dependent charge separation mechanisms that result in completely opposite photogenerated reactive sites (e^- and h^+) and divergent energy flows on the hybrid nanocatalysts. We find that plasmon-induced hot electrons in Au are injected into the conduction band of the CdS semiconductor nanorod. The specifically designed Au-tipped CdS heterostructures with a unique geometry (two Au nanoparticles at both ends of each CdS nanorod) provide more convincing high-resolution single-turnover mapping results and clearly prove the two charge separation mechanisms. Engineering the direction of energy flow at the nanoscale can provide an efficient way to overcome important challenges in photocatalysis, such as controlling catalytic activity and selectivity. These results bear enormous potential impact on the development of better visible light photocatalysts for solar-to-chemical energy conversion.

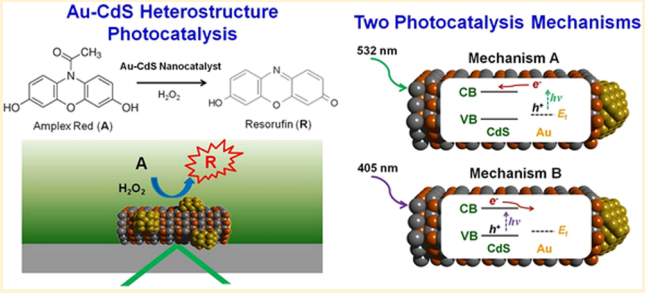

INTRODUCTION

Anisotropic semiconducting nanoparticles with high surface-to-volume ratios have gained much attention over the past decade as photocatalysts for many chemical reactions including photoelectrochemical hydrogen production[1−6] and photochemical degradation of organic pollutants.[7] Most semiconductor photocatalysts are currently based on wide-gap materials that have limited applicability outside of the UV range. However, UV light constitutes less than 5% of the solar spectrum; therefore, it is highly desirable to investigate photocatalysts with tunable activity that can be widely applied under visible light.

Metal-modified semiconductor nanorods are promising visible-active heterostructured photocatalysts for the following reasons: First, semiconductor nanorods, as compared to spherical semiconductors, provide the advantage of multiple exciton generation and more efficient photoinduced charge separation.[8,9] Second, the physical spatial separation of photogenerated electrons and holes in metal−semiconductor heterostructures can suppress recombination and enhance overall photocatalytic efficiency.[10] Third, recent advances in solution-phase synthesis enable the highly predictable and reliable fabrication of metal−semiconductor heterostructures with controlled size, shape, and composition tailored for specific applications.[11−13] Importantly, this unique ability to selectively build metal−semiconductor heterostructures with several morphologies and spatial relationships between their individual components can be used to engineer and direct energy flows at the nanoscale. This is a great advantage over their separate isolated components because one can conveniently tune the catalytic efficiency of the heterostructure by controlling the size, distribution, and loading of metal particles. In this context, it is important to elucidate the fundamental photocatalytic mechanisms operating on metal−semiconductor hybrid heterostructures to design and develop better (more active, selective, and stable) photocatalysts.

The photocatalytic behavior of metal−semiconductor heterostructures active in the visible has been studied mainly at the ensemble level.[14−21] For example, Amirav and Alivisatos demonstrated photocatalytic hydrogen production using Pt-tipped CdS nanorod heterostructures;[18] notably, the catalytic properties were considerably influenced by the individual particle sizes, structures, and so forth. To surmount the challenge arising from the intrinsic heterogeneity associated from ensemble-averaged measurements, it is highly desirable and necessary to employ photocatalytic measurements at the single-particle level.

Recently, single-particle catalysis using methods such as electrochemical detection,[22] surface plasmon spectroscopy,[23−25] and single-molecule fluorescence microscopy[26−33] has been demonstrated. Novo et al. reported the direct observation of oxidation reactions on single Au nanocrystals using dark-field microscopy.[23] Xu and co-workers presented the catalytic properties of Au nanoparticles at the single-particle level using single-molecule fluorescence microscopy.[29,30]

Received: August 30, 2013
Published: January 12, 2014

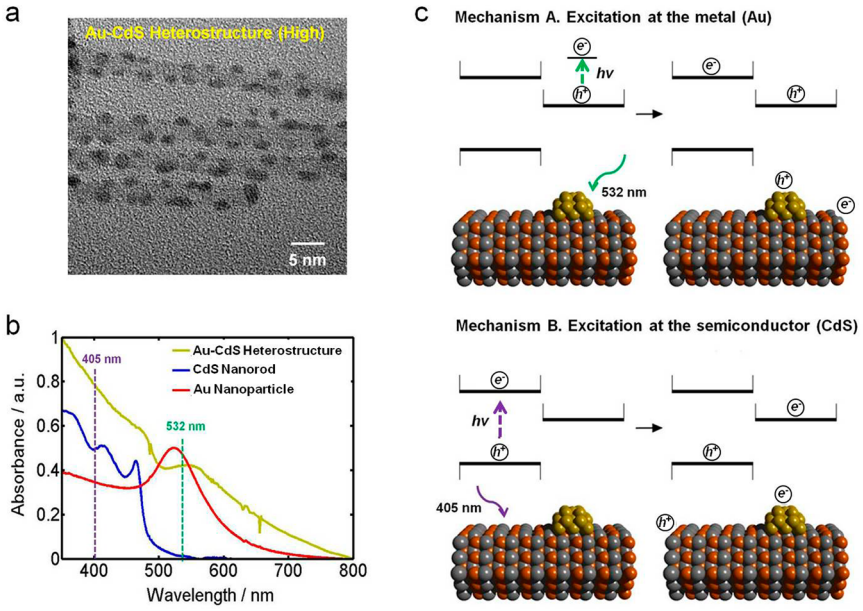

Figure 1. Photocatalytic Au−CdS hybrid heterostructures reveal two distinct photoinduced charge separation mechanisms. (a) TEM image of single high Au−CdS heterostructures (10.8 wt %). The CdS nanorods are 186(±56) nm long and 6.0(±0.9) nm wide. The diameter of Au nanoparticles ranges from 2 to 7 nm. (b) UV−vis absorption spectra of pure CdS nanorods (blue curve), Au nanoparticles (red curve), and high Au−CdS heterostructures (10.8 wt %, yellow curve). The green- and purple-dotted lines indicate the excitation source of a 532 nm laser and a 405 nm laser, respectively. (c) Two charge separation mechanisms in these hybrid heterostructures. Mechanism A starts by excitation at the metal at 532 nm, thus forming hot electrons (e^-) and holes (h^+) in the metal. The hot electrons are then transferred to the semiconductor's conduction band. Mechanism B starts with excitation at the semiconductor at 405 nm, thus forming electron−hole pairs at the semiconductor. Photogenerated electrons are then trapped by the gold metal.

Roeffaers et al. used single-molecule fluorescence microscopy to monitor single turnover reactions catalyzed by crystals of a layered double hydroxide (LDH).[33] Furthermore, high-resolution superlocalization fluorescence imaging in single-particle catalysis has also been carried out by several groups.[32,34−36] Zhou et al. employed superlocalization fluorescence imaging to unveil the surface reactivity of Au nanorod catalysts, and found that surface defects play important roles in catalytic activity.[32] De Cremer et al. reported high-resolution reactivity mapping of epoxidation reactions catalyzed by mesoporous titanosilicates.[35]

More recently, superlocalization fluorescence imaging of single metal−semiconductor heterostructures has been demonstrated by Tachikawa et al.; in this report, single-molecule super-resolution imaging of reactive sites on single Au-TiO_2 hybrid particles were studied using an oxidation−reduction (redox)-responsive fluorescent dye.[34] Despite the recent study of photocatalysis by Au−TiO_2 hybrid particles at the single-particle level, the proposed mechanisms of action have not been clearly verified experimentally, and it is still necessary to develop metal−semiconductor heterostructures that can be fully operated with tunable activity under visible light. Further, many photocatalytic properties such as selectivity in metal−semiconductor heterostructures remain largely unanswered, and our understanding of the identity of the surface reactive sites and factors affecting the catalytic efficiency in these hybrid materials is still very limited. Therefore, the remaining grand challenges in this area are to experimentally verify mechanisms of action in metal−semiconductor heterostructures, to investigate and develop highly active metal−semiconductor heterostructures with tunable activity under visible light, to resolve the single surface reactive sites where individual photoinduced redox reactions occur on these photocatalytic structures, and to clarify the factors that control catalytic activity and selectivity in metal−semiconductor heterostructures.

To address the aforementioned challenges, we synthesized CdS semiconductor nanorods decorated with Au nanoparticles and studied the real-time redox photocatalysis of these hybrid heterostructures at the single-particle level with millisecond time resolution. We chose Au−CdS hybrid heterostructures as photocatalysts because they provide efficient light absorption and photocatalytic activity in the visible range.[37] We employ high-resolution superlocalization fluorescence imaging to resolve the nature and photocatalytic properties of the photogenerated carriers and redox reactive sites (electrons, e^- and holes, h^+) in Au−CdS hybrid heterostructures, using single-molecule detection following the oxidation of nonfluorescent amplex red to highly fluorescent resorufin. Moreover, we verify two distinct, incident energy-dependent charge separation mechanisms using specifically designed Au-tipped CdS heterostructures. We further provide a new insight into the working mechanism of photocatalysis (driven by light in Au and CdS) and surface catalysis (driven by Au surface) in the Au−CdS heterostructures during the fluorogenic oxidation reaction.

RESULTS AND DISCUSSION

Two Charge Separation Mechanisms in Au−CdS Heterostructures. Au−CdS hybrid heterostructures used here were synthesized according to modified literature procedures (see details in the Supporting Information).[38,39] Figure 1a shows a transmission electron microscopy (TEM) image of single CdS nanorods densely decorated with Au nanoparticles ("high" surface-Au density). The diameter of the Au nanoparticles ranged from 2 to 7 nm, and the Au loading on

dx.doi.org/10.1021/ja409011y | J. Am. Chem. Soc. 2014, 136, 1398−1408

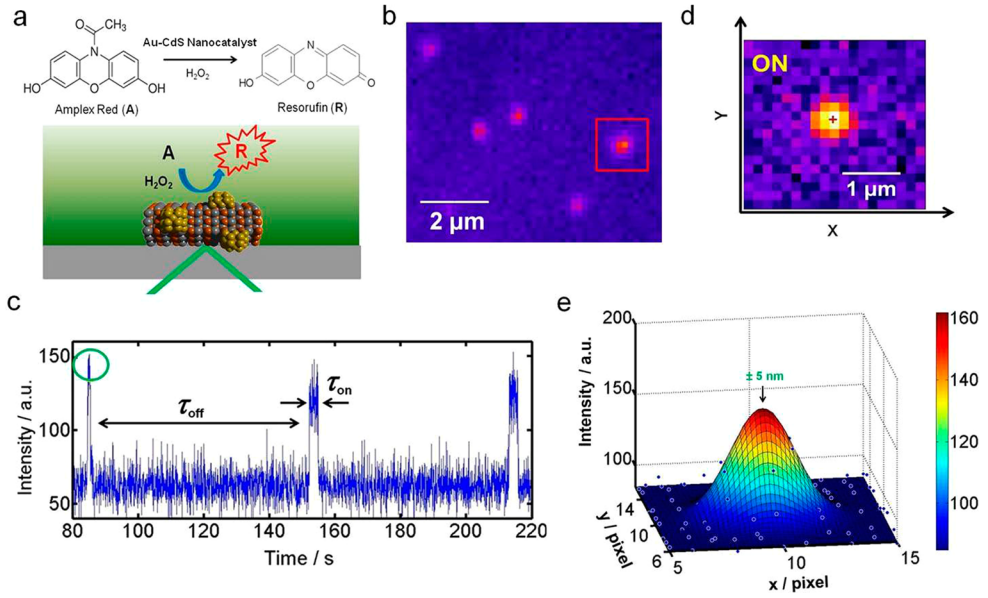

Figure 2. Single-molecule superlocalization fluorescence imaging over single Au−CdS heterostructures during a photocatalytic oxidation reaction. (a) Experimental scheme using total internal reflection fluorescence microscopy to probe the fluorogenic oxidation reaction of nonfluorescent amplex red (A) to highly fluorescent resorufin (R) by a Au−CdS nanocatalyst. (b) Typical image of fluorescent products at localized spots during the catalytic reaction under 532 nm illumination. (c) Segment of a typical fluorescence intensity trajectory from the fluorescent spot squared in red in b with 1 μM amplex red, 20 mM H_2O_2, and 10 mM phosphate buffer (pH 7.5). Temporal resolution is 50 ms. (d) Fluorescence image of a single resorufin molecule during one burst circled in green in (c). (e) Three-dimensional representation of the image in (d). The center position of the fluorescence image can be determined with nanometer accuracy (±5 nm) and is marked as a red cross in (d).

the CdS nanorod was calculated to be about 10.8 wt %. The mean length and diameter of CdS nanorods used in this study were 186(±56) nm and 6.0(±0.9) nm, respectively (Figures S1 and S2).

In Au−CdS hybrid heterostructures, the optical properties of the original components are essentially retained.[40] Hence, the optical absorption spectra of Au−CdS heterostructures exhibit both the characteristic excitonic and continuous absorption of the CdS nanorods below 475 nm (2.61 eV), together with an additional broad absorption centered around 532 nm (2.33 eV) due to the plasmonic Au nanoparticles (Figure 1b). This can be ascribed to the separate optical excitations of the semiconductor and metal components in the hybrid material. This is advantageous because it enables to separately probe each one of the two heterostructure components using two different incident light wavelengths.

Because of the separation of the plasmonic and excitonic features in Au−CdS hybrid heterostructures, two distinct photoinduced charge separation mechanisms are expected to exist depending on the incident excitation energy as shown in Figure 1c. Mechanism A starts with 532 nm absorption by the gold metal, followed by the formation of d-band electron−hole pairs excited above the Fermi level upon decay of surface plasmons in the metal. Excited plasmonic nanoparticles that are much smaller than their plasmon resonance wavelength can be an efficient source of hot electrons (e^-) and holes (h^+).[41,42] The hot electrons have energies between vacuum level and the work function ϕ of gold metal (ϕ = 4.83 eV).[41,43] These energetic electrons could be potentially used in photochemistry.[41,42,44−46] For example, Mukherjee et al. recently demonstrated that hot electrons formed on Au nanoparticles can be used for the room temperature dissociation of H_2, which requires a dissociation enthalpy of 436 kJ/mol (4.51 eV).[41] A significant fraction of the energetic electrons in Au nanoparticles can either overcome the energy barrier (Schottky junction) at the metal−semiconductor interface or tunnel through it to become conduction electrons in the semiconductor.[34,47,48] This results in a spatially separated electron−hole pair where the electron resides in the semiconductor (CdS), whereas the hole remains in the metal (Au). Mechanism B starts with 405 nm absorption by the semiconductor, followed by charge transfer of photoexcited electrons to the metal. The electrons transferred to the Au metal increase the electron density within the Au nanoparticles, thus shifting the Fermi level toward more negative potentials.[49] The transfer of electrons to the metal continues until the Fermi level equilibrates with the conduction band edge of the semiconductor.[49] In contrast to the previous mechanism A, mechanism B (405 nm excitation) charges the gold negatively and the CdS semiconductor positively. In other words, mechanisms A and B result in two different charge-separated Au−CdS species of completely opposite polarity. So far, mechanism B is well established and widely used in photocatalytic chemistry.[3,15] However, mechanism A is still poorly understood in nanocatalysis. Therefore, in the present study, we first try to experimentally verify the existence and catalytic activity of mechanism A in these Au−CdS hybrid heterostructures using 532 nm excitation, and further investigate the capability to optically control the direction of energy flow together with the catalytic activity and selectivity offered by these two mechanisms as depicted in Figure 1c.

Catalytic Activity of Au−CdS Heterostructures in Fluorogenic Oxidation Reactions. To test and study the two aforementioned charge separation mechanisms in Au−CdS hybrid heterostructures, we used the fluorogenic oxidation reaction of nonfluorescent amplex red (10-acetyl-3,7-dihydroxyphenoxazine) to produce highly fluorescent resorufin (λ_{exc} = 563 nm; λ_{em} = 587 nm, at pH 7.5).[31,32] Experimentally, we first tested if high Au−CdS heterostructures (Figure 1a) were active

dx.doi.org/10.1021/ja409011y | J. Am. Chem. Soc. 2014, 136, 1398−1408

in catalyzing the oxidation of amplex red to resorufin by ensemble-averaged measurements. An aliquot of a solution containing Au−CdS heterostructures was injected into a cuvette containing a solution of 1 μM amplex red, 20 mM H_2O_2, and 10 mM phosphate buffer with pH 7.5. The cuvette was illuminated at 532 nm (±25 nm band-pass filter), and the fluorescence intensity was measured every 30 s of continuous illumination. As shown in Figure S3, the fluorescence intensity arising from resorufin increases as a function of time in the presence of high Au−CdS heterostructures, but remains constant in the absence of high Au−CdS heterostructures under the same conditions. This indicates that the Au−CdS heterostructures are active for the fluorogenic oxidation reaction under mechanism A at 532 nm. We estimate about 39% of resorufin product is produced in 15 min under the specified conditions (Figure S3).

To better understand the photocatalytic properties of the Au−CdS hybrid heterostructures, we performed the same fluorogenic oxidation reaction at the single-particle level. A sample was prepared by spin-casting Au−CdS heterostructure solution on a positively functionalized quartz slide. The concentration of the Au−CdS heterostructures immobilized on the quartz slide was controlled to be ~1 μm^{-2} for single-particle catalysis and was checked using a differential interference contrast (DIC) microscope (Figure S4). The sample slide was then measured under a prism-type dual-color total internal reflection fluorescence (TIRF) microscope (Figure S5). A 532-nm green laser was used to excite both the metal in Au−CdS heterostructures and the fluorescent resorufin product. Before initiating the fluorogenic oxidation reaction, we first shined the 532-nm laser beam onto the sample for 20 min to remove possible fluorescent dusts or impurities. We then introduced the reactant-containing solution (1 μM amplex red, 20 mM H_2O_2, 10 mM pH 7.5 phosphate buffer) over the Au−CdS heterostructures within a flow chamber. A highly fluorescent resorufin product was formed at one of many possible reactive sites on a single Au−CdS heterostructure (Figure 2a), and was detected by an electron-multiplying charge-coupled device (EMCCD) camera (Figure S5b). The resorufin product (pK_a = 5.8) is deprotonated and negatively charged in the solution with pH = 7.5. We recorded movies of stochastic fluorescence bursts at many localized spots on the quartz surface with a time resolution of 50 ms (Figure 2b). Figure 2c shows a segment of a typical fluorescence intensity trajectory from one spot squared in red in Figure 2b containing stochastic fluorescence ON−OFF signals. If these signals were produced from multiple resorufin molecules we would expect a distribution of variable intensity fluorescent signals, but the consistent height of the two-state ON-level in Figure 2c indicates that each fluorescence burst comes from a single resorufin molecule. Figure 2d is a fluorescence image of a single resorufin molecule during one burst circled in green in Figure 2c and the fluorescence intensity of a single resorufin molecule spread over a few pixels as a point spread function (PSF). The center position of this PSF can be determined with nanometer accuracy by two-dimensional (2D) Gaussian fitting of its fluorescence profile (Figure 2e). This enables us to localize the position of every resorufin molecule on a single Au−CdS heterostructure during the catalytic reactions. In this study, red-fluorescent beads with a diameter of 100 nm were used as position markers to correctly localize the position of each resorufin molecule (Figures S6 and S7).

To further confirm that each fluorescence burst comes from a single turnover catalytic reaction of amplex red over Au−CdS heterostructures, we carried out further control experiments at the single-particle level. We observed no stochastic fluorescence bursts over Au−CdS heterostructures in the absence of amplex red reactant or over pure CdS nanorods while the rest of the experimental conditions were kept constant. In addition, no digital single-molecule fluorescence bursts were observed over Au−CdS heterostructures with resorufin product in solution under the same conditions. There are three important findings from these control experiments. First, a 532 nm green laser does not excite isolated metal-free CdS nanorods, which means that the intensity signal observed during catalysis is only contributed from Au-modified heterostructures under mechanism A at 532 nm. Second, our Au−CdS heterostructures do not exhibit any time-dependent emission fluctuations (or blinking) that could affect fluorescence bursts or our data analysis (see more detailed discussion on blinking in the Supporting Information). This is further verified by our previous report to show no fluorescence emissions of CdS nanorods with aspect ratios greater than 3 due to exciton quenching by surface defects.[50] Third, our results indicate that diffusion of free resorufin in solution does not yield any significant fluorescence bursts through its binding to the nanoparticles under our experimental conditions (see more details in the Supporting Information). This is also verified by previous reports carried out under similar experimental conditions.[29,31] Furthermore, every product formation (or dissociation) event in each single-molecule fluorescence trajectory (Figure 2c) appears as a sudden increase (or decrease) in intensity. In contrast, Xu et al. demonstrated that photobleaching of single resorufin molecules happens on much longer time scales (~25 s) under similar 532 nm laser intensities.[29] This strongly indicates that each observed sudden decrease in intensity is attributed to the dissociation of adsorbed resorufin from the reactive site where it is produced. Therefore, the fluorescence bursts observed in this study are attributed to the oxidation of amplex red to fluorescent resorufin at reactive sites on single Au−CdS heterostructures, and each fluorescence burst corresponds to a single catalytic turnover that results in the formation of one resorufin molecule at a reactive site, followed by its subsequent dissociation away from that reactive site on a Au−CdS heterostructure.

Photocatalysis and Surface Catalysis Responsible for Activity of Au−CdS Heterostructures. We showed that the Au−CdS heterostructures are active for the fluorogenic oxidation reaction under mechanism A at 532 nm. However, Zhou et al. have demonstrated that isolated, unmodified (CdS-free) Au nanoparticles mediate the oxidation of amplex red to resorufin by surface catalysis.[32] Therefore, it is important to ensure that photocatalytic mechanism A, involving excited surface plasmons on Au followed by charge separation into the CdS semiconductor, was actually operating and was responsible for activity under 532 nm illumination. For this purpose, we performed several ensemble experiments (see more details in Supporting Information). Among key results from these experiments, we found that the absorbance due to resorufin product builds up about 4 times faster under continuous 532 nm illumination than it does in the dark (only surface catalysis) as shown in Figure S8. We also corroborated that 532 nm green light cannot excite pure (metal-free) CdS nanorods; this supports a null (zero) contribution to activity from the CdS nanorods alone via mechanism A at 532 nm in the presence of

dx.doi.org/10.1021/ja409011y | J. Am. Chem. Soc. 2014, 136, 1398−1408

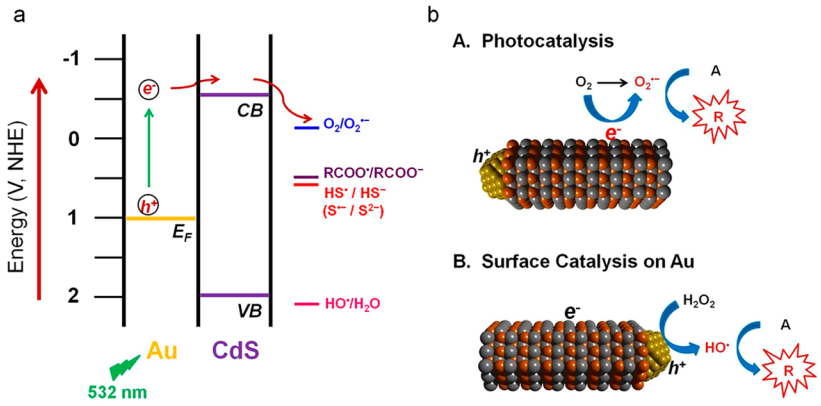

Figure 3. Photocatalysis and surface catalysis in Au−CdS heterostuctures under mechanism A at 532 nm. (a) Approximate energy band positions of the Fermi level (E_F) of bulk Au and the conduction band (CB) of CdS. The redox potentials of some of molecules are shown on the right side. The energy scale is indicated using the normal hydrogen electrode (NHE). A more detailed energy level diagram is provided in Figure S11. (b) Schematics depicting the formation of resorufin product (R) from amplex red (A) in photocatalysis (top) and surface catalysis (bottom).

the heterostructures (Figures S9 and S10). These results clearly indicate that the surface-bound Au nanoparticles become excited and make the Au−CdS heterostructures distinguishably more active under 532 nm illumination.

Next, it is important to clarify how resorufin molecules are produced under photocatalytic mechanism A. For a wide band gap titanium dioxide (TiO_2) in an aqueous environment, photogenerated electrons (e^-) are known to reductively react with adsorbed oxygen (O_2) as the primary electron acceptor to generate surface-bound superoxide anion radicals ($O_2^{\bullet-}$).[51−54] In addition, photogenerated holes (h^+) oxidatively react with adsorbed water (H_2O) to generate surface-bound hydroxyl radicals ($HO^\bullet$).[52,53] Both of these two surface-bound oxygen radicals are known to be very reactive toward nonfluorescent amplex red, catalyzing its fluorogenic oxidation to fluorescent resorufin.[54,55] Therefore, we checked if these surface-bound oxygen radicals were responsible for the photocatalytic activity of Au−CdS heterostructures under mechanism A at 532 nm (Figure S8). Plasmon-induced hot electrons in Au upon 532 nm excitation can be transferred into the conduction band (CB) of CdS.[47,48,56] As shown in Figures 3a and S11, the CB energy E_{CB} for CdS is sufficiently negative to reduce O_2 to $O_2^{\bullet-}$.[57] This means that $O_2^{\bullet-}$ radicals can be produced in Au−CdS heterostructures under 532-nm illumination. However, photogenerated holes with the Fermi energy E_F in Au do not have sufficient energy to oxidize H_2O to $HO^\bullet$ because the E_F of Au is more negative than the energy for $HO^\bullet/H_2O$ reaction (Figures 3a and S11).[57] Therefore, the increase of activity by ∼4 times of Au−CdS heterostructures under 532 nm illumination in Figure S8d can be ascribed to the formation of reactive $O_2^{\bullet-}$ radicals followed by their reaction with amplex red to form resorufin product (Figure 3b, photocatalysis). Furthermore, we also need to consider the effect of charge separation (e^- in CdS and h^+ in Au) on the activity of Au−CdS heterostructures. Recently, Wu et al. reported that the charge-separated state is relatively short-lived for short Au−CdS heterostructures.[56] However, our long Au−CdS heterostructures (186 nm × 6 nm on average) may slow down the charge recombination through the formation of Au−CdS Schottky barrier that expels electrons away from the interface.[56] In this respect, it is expected that the charge-separated state will be relatively longer-lived in our Au−CdS heterostructures under mechanism A, and the charge separation can have significant influence on their catalytic activity. To clearly verify this, we performed further ensemble-averaged experiments using 5 nm Au nanoparticles (no charge separation) under 532 nm illumination (Figures S12 and S13). As shown in Figure S13, the fluorescence intensity was increased by 0.085 in Au−CdS heterostructures with charge separation when compared to Au nanoparticles without charge separation under 532 nm illumination. The increase by 0.085 is ascribed to the charge separation in Au−CdS heterostructures. Furthermore, the fluorescence intensity was found to be increased by 0.025 from Au−CdS heterostructures under dark conditions to Au nanoparticles under 532 nm illumination. The fluorescence increase by 0.025 can be ascribed to the photocatalysis involving $O_2^{\bullet-}$ radicals and heating effect by Au. Therefore, we found that the charge separation have considerable impact on the activity of Au−CdS heterostructures, while photo-induced heating effect by Au nanoparticles does not have as significant an impact on the activity under 532 nm illumination (see details in the Supporting Information).

So far, we verified the existence and activity of photocatalytic mechanism A in Au−CdS heterostructures under 532 nm excitation. However, it is also important to take a closer look at the aforementioned surface catalysis (Figure S8c, dark) that also contributes to the activity of Au−CdS heterostructures under mechanism A. Although surface catalysis on Au was reported by Zhou et al.,[32] our understanding of the detailed mechanism is still limited. We therefore performed ensemble-averaged experiments to better understand the working mechanism behind surface catalysis on Au nanoparticle. Amplex red used in this study has been widely used as sensitive fluorogenic probes to detect horseradish peroxidase (HRP) and H_2O_2 in many immunoassays.[58,59] Amplex red, in the presence of HRP, reacts with H_2O_2 to produce highly fluorescent resorufin. More specifically, HRP is used as a catalyst to convert H_2O_2 into $HO^\bullet$ radicals, followed by their reaction with amplex red to form resorufin.[54] Similarly, it is reported that Au nanoparticles used as a catalyst in this study can also decompose H_2O_2 into $HO^\bullet$ radicals on their surfaces.[60] Therefore, it is expected that resorufin product could be formed by the reaction of amplex red with $HO^\bullet$ radicals generated from H_2O_2 in the presence of Au as described in Figure 3b (bottom). From our ensemble experiments, we found that H_2O_2 is directly related to the activity of surface catalysis on Au (Figure S14). This result suggests that surface catalysis on Au happens in the presence of H_2O_2 and that reactive $HO^\bullet$

dx.doi.org/10.1021/ja409011y | J. Am. Chem. Soc. 2014, 136, 1398−1408

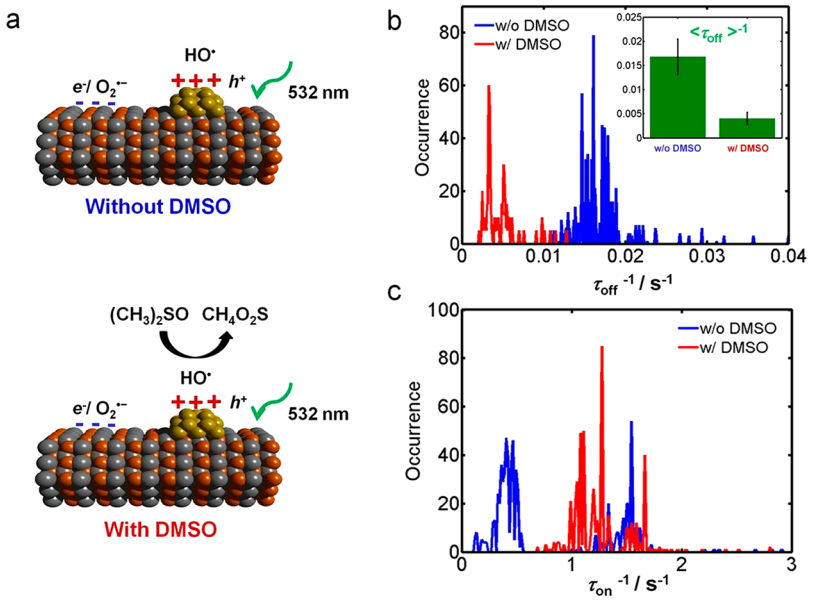

Figure 4. Heterogeneous and distinct photocatalytic activity of reactive sites on Au−CdS heterostructures. (a) Two distinct microenvironments around two different reactive sites (e^- and h^+) under 532 nm excitation. The reactive sites around photogenerated holes have a positively charged microenvironment, while the reactive sites around photogenerated electrons have a negatively charged microenvironment. In this study, dimethyl sulfoxide (DMSO) is used to quench the HO• radicals (or suppress the surface catalysis on Au). DMSO is oxidized by the HO• radicals to methanesulfinic acid (MSIA, CH_4O_2S). (b) Histogram of the rate of product formation τ_{off}^{-1} for the fluorescence bursts obtained from over 100 individual nanoparticles in the absence of DMSO (blue curve) or in the presence of DMSO (red curve). (c) Histogram of the rate of product dissociation τ_{on}^{-1} for the fluorescence bursts obtained in the absence of DMSO (blue curve) or in the presence of DMSO (red curve). The distinct dissociation kinetics of the two basic reactive sites are observed because of the differently charged microenvironments as depicted in (a).

radicals may be involved as an intermediate in the oxidation reaction. Further verification and discussion on the formation of HO• radicals in surface catalysis is described in the following section.

Two Distinct Dissociation Kinetics in Single-Molecule Experiments. In the fluorescence intensity trajectory, photocatalytic events have two important characteristic durations, τ_{off} and τ_{on} (Figure 2c); τ_{off} is the characteristic time before the formation of a fluorescent product on the Au−CdS heterostructure, and τ_{on} is the characteristic time related to the dissociation of the product molecule from the nanocatalyst surface. The inverse of the values of τ_{off} and τ_{on} represent the single-reactive site rates of product formation and of product dissociation, respectively. Therefore, a higher value of τ_{on}^{-1} indicates faster dissociation of the resorufin product, while a higher value of τ_{off}^{-1} indicates faster formation of the resorufin product.

It is important to note that some fluorescence bursts show long τ_{on} values of 2−6 s, while other fluorescence bursts show short τ_{on} values of 0.3−1.2 s (Figure 2c). We believe that these two distinct τ_{on} values can be ascribed to two charge-separated species containing photogenerated carriers at different locations and microenvironments (Figures 1c and 4a). In this experiment (mechanism A at 532 nm), the reactive sites around photogenerated electrons (the e^- reactive sites) have a negatively charged microenvironment which can promote quicker dissociation of negatively charged resorufin molecule due to the repulsive electrostatic force (Figure 4a).[31] In comparison, the reactive sites around photogenerated holes (or the h^+ reactive sites) have a positively charged microenvironment which can enhance the adsorption of the negatively charged resorufin product (Figure 4a).[31]

To clearly verify the aforementioned reactive sites and the formation of HO• radicals in surface catalysis on Au, we used dimethyl sulfoxide (DMSO, 20 mM) known to get oxidized by HO• radicals to form the stable compound methanesulfinic acid (MSIA, CH_4O_2S).[61,62] If HO• radicals are actually involved in surface catalysis on Au, the surface catalysis will be suppressed in the presence of DMSO under mechanism A at 532 nm, and it is expected that fluorescence bursts should come from the e^- reactive sites only.

Figure S15a shows a segment of a fluorescence intensity trajectory over one Au−CdS heterostructure in the absence of DMSO and the time profile for the two rates for each fluorescence burst. We observe that the rates of product formation and product dissociation over the same heterostructure vary at different times. Figure S15b shows a segment of a fluorescence intensity trajectory over one Au−CdS heterostructure in the presence of DMSO and the time profile for the two rates for each fluorescence burst. From these experiments, it is clear there is heterogeneity in catalytic activity among the e^- reactive sites on the same Au−CdS heterostructure. This previously unobserved trait is always masked in the ensemble-averaged measurements. More importantly, as compared to the fluorescence bursts in the absence of DMSO (Figure S15a), all the fluorescence bursts in the presence of DMSO (Figure S15b) show τ_{on}^{-1} values higher than 0.6 s^{-1}, where the averaged rate of product dissociation $\langle\tau_{on}\rangle^{-1}$ is 1.18 s^{-1} over a single Au−CdS heterostructure. This suggests that the lower τ_{on}^{-1} value of around ∼0.25 s^{-1} in Figure S15a could be ascribed to the h^+ reactive sites around a positively charged microenvironment in Au. More importantly, the result further suggests that HO• radicals are involved in the fluorogenic oxidation reaction as described in Figure 3b (bottom). Nevertheless, the individual τ_{on}^{-1} and τ_{off}^{-1} values

dx.doi.org/10.1021/ja409011y | J. Am. Chem. Soc. 2014, 136, 1398−1408

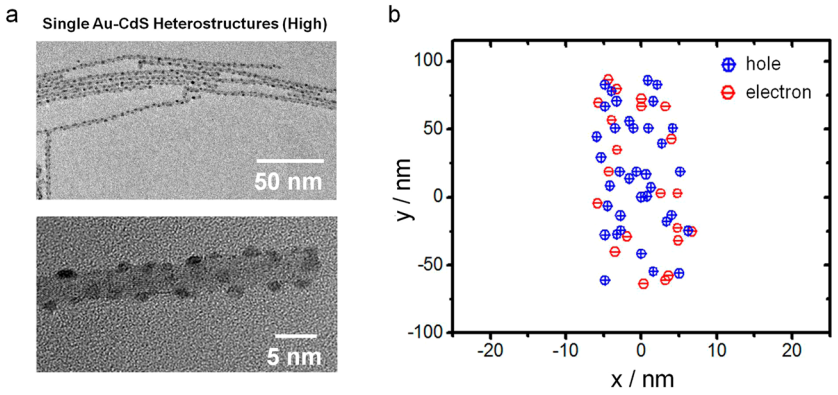

Figure 5. Superlocalization of single surface reactive sites on a high Au−CdS heterostructure during photocatalysis. (a) TEM image of typical single high Au−CdS heterostructures (top). Enlarged TEM image (bottom) shows high density of Au nanoparticles. (b) Super-resolution mapping of individual reactive sites on a high metal loading Au−CdS heterostructure at 532 nm. Each one of the circled cross or minus signs corresponds to one resorufin product molecule. The circled blue crosses show a product molecule caused by the h^+ reactive sites on Au, while the circled red minuses shows a product molecule from the e^- reactive sites. The catalytic reaction was carried out with 1 μM amplex red and 20 mM H_2O_2 in 10 mM pH 7.5 phosphate buffer.

in single-molecule events are stochastic, and hence, their statistical properties, such as average values and distributions, are required to draw a more concrete and meaningful conclusion about the distinct dissociation kinetics in single-molecule experiments.

To more clearly elucidate the distinct dissociation kinetics between the two different reactive sites, we further measured many more Au−CdS hybrid heterostructures for both cases (with and without DMSO). In each case, we collected many fluorescence bursts from over 100 individual nanoparticles for a statistical analysis. Figure 4b shows a histogram of the rate of product formation for all the fluorescence bursts. We found that the averaged rate of product formation $\langle\tau_{off}\rangle^{-1}$ is 0.0168 s^{-1} in the absence of DMSO, while $\langle\tau_{off}\rangle^{-1}$ in the presence of DMSO is 0.00403 s^{-1}. This difference in the averaged rate of product formation can be explained by the effect of DMSO competing with, and hindering amplex red near the nanocatalyst surface, thus suppressing the surface catalysis on Au. This DMSO effect is further verified by ensemble experiments (Figure S16). In addition, Figure 4c shows a histogram of the rate of product dissociation for all the fluorescence bursts. Interestingly, we find that the rate of product dissociation τ_{on}^{-1} obtained without DMSO has two distinct distributions (or peaks) for individual fluorescence bursts (Figure 4c), which is not observed in the presence of DMSO. Therefore, Figure 4c verifies that the fluorescence bursts yielding the lower τ_{on}^{-1} of around 0.25 s^{-1} on the left side of the distribution come from the h^+ reactive sites, while the fluorescence bursts yielding the higher τ_{on}^{-1} around 1.2 s^{-1} on the right side of the distribution arise from the e^- reactive sites. The distinct dissociation kinetics for the two different reactive sites are further supported by a recent report.[31]

High-Resolution Mapping of Single Turnover Events on Au−CdS Heterostructures. The finding on the two distinct dissociation kinetics is important because we can directly distinguish catalytic fluorescence bursts caused by the h^+ reactive sites from those by the e^- reactive sites in a fluorescence intensity trajectory. More importantly, this allows for resolving individual electron and hole transfer events following photoinduced charge separation in single Au−CdS hybrid heterostructures. We thus tried to map the individual reactive sites on a single high Au−CdS heterostructure (10.8 wt % Au) under 532 nm laser excitation for 60 min through localizing the position of every resorufin molecule with nanometer accuracy (Figure 5; see more details on superlocalization of the center position in the Supporting Information). Figure 5a shows TEM images of typical single Au−CdS heterostructures with high metal loading, showing that the Au nanoparticles are deposited and distributed along the length of the CdS nanorod. Figure 5b is a super-resolution image mapping single surface reactive sites during the photocatalytic oxidation reaction on a Au−CdS hybrid heterostructure with a similarly high metal loading. Plasmon-induced energetic electrons (encircled-marked as red minuses), initially created in the metal particles, are injected into the conduction band of the CdS semiconductor nanorod. Therefore, our experimental results are consistent with the existence of mechanism A involving photoinduced charge transfer from the gold metal to the CdS semiconductor under 532 nm light. To the best of our knowledge, this is the first report resolving and mapping individual reactive sites on single Au−CdS hybrid heterostructured photocatalysts using a high-resolution superlocalization imaging technique.

Photocatalytic Mechanism B in Au−CdS Heterostructures. It is also important to check the photocatalytic activity of CdS nanorods under mechanism B (Figure 1c). We therefore tried to verify the existence of mechanism B involving photogenerated electrons and holes in CdS nanorods at the ensemble level. We checked if pure (metal-free) CdS nanorods can catalyze the oxidation reaction of amplex red to resorufin, which is necessary to support the existence of mechanism B (see more details in the Supporting Information). In the presence of CdS nanorods, the resorufin product's absorption maximum at 573 nm increased with an interval of 30 s, while it remained constant in the absence of CdS nanorods under identical conditions (Figure S17). This result clearly shows that the resorufin product is also formed through photocatalysis under mechanism B (Figures S17d and S18).

We further elucidate the formation of reactive radicals responsible for photocatalytic activity under mechanism B in CdS nanorods. As shown in Figure S11, $O_2^{\bullet-}$ radicals can be produced in CdS nanorods under mechanism B, while photogenerated holes in CdS do not have enough energy to react with H_2O to produce $HO^{\bullet}$ radicals (see details in the

dx.doi.org/10.1021/ja409011y | J. Am. Chem. Soc. 2014, 136, 1398−1408

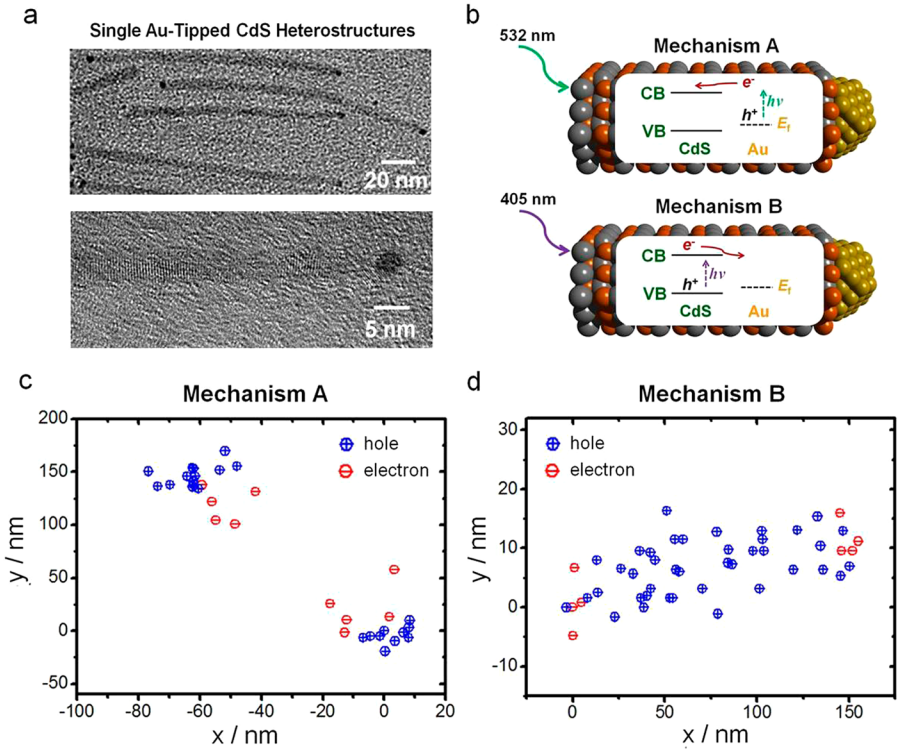

Figure 6. Engineering energy flows on single Au-tipped CdS nanorod heterostructures. (a) TEM image of typical single Au-tipped CdS nanorod heterostructures (top). Enlarged TEM image (bottom) shows a Au nanoparticle at the tip. (b) Schematic illustrating two distinct photocatalysis mechanisms with the opposite direction of energy flow (opposite polarity after photoinduced charge-separation). In mechanism A at 532 nm, the photogenerated energetic electrons in the gold metal are injected to the conduction band (CB) of the semiconductor. In mechanism B at 405 nm, the photogenerated electrons in the CB of the semiconductor are rapidly trapped by the gold metal. (c) Super-resolution mapping of single reactive sites on a Au-tipped CdS nanorod heterostructure during the oxidation reaction at 532 nm (mechanism A). (d) Super-resolution mapping of single reactive sites on a Au-tipped CdS nanorod heterostructure during the same oxidation reaction after turning on the 405 nm laser (in addition to the 532 nm laser, needed to excite the resorufin product) (mechanism B).

Supporting Information). However, we observed that pure (metal-free) CdS nanorods are still active in the presence of superoxide dismutase (SOD) to quench $O_2^{\bullet-}$ radicals (Figure S19). This strongly indicates that another radical species are produced from holes generated in CdS. We found that photogenerated holes in CdS have enough energy to react with some of the ligands (S^{2-} (or HS^-) and $RCOO^-$) present in high concentrations on the surface of the CdS nanorod (Figures 3a and S11).[57,63−66] These reactions can easily generate highly reactive radical species such as $S^{\bullet-}$ (or $HS^{\bullet}$) (sulfanyl) and $RCOO^{\bullet}$ (carboxyl),[63−65] each of which can in turn be responsible for the oxidation of amplex red to the fluorescent resorufin product.[66−68] Therefore, under mechanism B, $O_2^{\bullet-}$ radicals can be generated from electrons, while $S^{\bullet-}/HS^{\bullet}$ or $RCOO^{\bullet}$ radicals are expected to be produced from holes.

Verification of Two Charge Separation Mechanisms on Au-tipped CdS Heterostructures. To clearly demonstrate the existence of two distinct photocatalysis mechanisms having the opposite direction of energy flow (i.e., having the opposite polarity after photoinduced charge separation) at the single-particle level, we further synthesized Au-tipped CdS heterostructures (Figures 6a and S1a). The specifically designed Au-tipped CdS heterostructures are visible-active photocatalysts with a unique geometry: two Au nanoparticles at both ends of each CdS nanorod. The 5−15 nm superlocalization accuracy typically found in single-molecule superlocalization studies can make it very challenging to pinpoint the turnover events on a nanoscale particle. However, in our study, the relatively long distance between the two Au nanoparticles (186 nm on average) allows us to avoid this pitfall, and the unique geometry enables us to clearly prove the two charge separation mechanisms with the opposite direction of energy flow.

An absorption spectrum of Au-tipped CdS heterostructures is provided in Figure S20. These Au−CdS heterostructures differed from those mentioned above in that they have a very low metal loading (0.54 wt % Au on CdS). As depicted in Figure 6b, we can selectively excite either the gold metal domains at 532 nm to turn ON mechanism A, or the CdS semiconductor nanorod domains at 405 nm to turn ON mechanism B. We note however, that under single-molecule experiments presented here, a 532-nm laser was always needed to excite resorufin product, and both 405 and 532 nm lasers were used in our study of mechanism B. Figure 6c shows a super-resolution image mapping the reactive sites during the same amplex red to resorufin oxidation reaction taken at 532 nm over 1 h. Interestingly, we find that the h^+ reactive sites (circled blue-cross) are positioned at the gold tips on both ends of the heterostructures, while the e^- reactive sites (circled red-minus) are located along the inside length of the CdS nanorods within a distance of a few tens of nanometers from the gold tips. Therefore, this result reveals that at 532 nm we turned ON mechanism A, which proceeds by charge (electron) transfer from the gold metal to the CdS semiconductor nanorod. This is consistent with our observations described above for the CdS nanorods with high Au loading (Figure 5b). In addition, Figure

dx.doi.org/10.1021/ja409011y | J. Am. Chem. Soc. 2014, 136, 1398−1408

6d shows a super-resolution image mapping the reactive sites obtained after turning on the 405 nm laser in addition to the 532 nm laser (the latter needed to excite the resorufin product). We ensured that CdS nanorods in this study are excited at 405 nm under a dual-color TIRF microscope (Figure S21). Critically, in this case the h^+ reactive sites (encircled blue-crosses) are distributed along the inside length of the CdS nanorod, while the e^- reactive sites (encircled red minuses) are located at both ends. Note that Fermi level equilibration can significantly raise the energy the level of small Au nanoparticles compared to bulk Au, closer to the conduction band of the CdS semiconductor.[49] This supports that the electrons transferred to the Au metal from the CdS semiconductor can have enough energy to react with O_2 to produce $O_2^{\bullet-}$ radicals (Figure S11). Efficient charge separation by the CdS nanorods could lead to a heterogeneous carrier distribution and compact location along the tips. However, the photogenerated carriers can travel along the CdS semiconductor nanorods, followed by their reaction to create and localize surface-bound radicals. It should be noted that although both mechanisms A and B are turned ON when using both 405 and 532 nm lasers, the super-resolution image (Figure 6d) clearly differs from the super-resolution image when using the 532 nm laser only (Figure 6c), revealing the existence of mechanism B: Charge (electron) transfer from the CdS semiconductor nanorod to the gold metal at the tip. We note that mechanism B dominates when both lasers are used. Given the similar power intensities, this observation indicates that photogenerated electrons and holes appear to be more active and longer-lived when generated at CdS than when generated at Au (see below).[56] Therefore, we have disclosed the existence of two distinct photocatalysis mechanisms in Au–CdS heterostructures. The photoinduced redox activity of these Au–CdS heterostructures can be selectively turned ON by two different mechanisms using two different wavelengths of incident light.

We also compared the rates of product formation and dissociation for mechanism A (532 nm) and mechanism B (405 and 532 nm) in Au-tipped CdS heterostructures during the photocatalytic oxidation reaction. We found that the averaged rate of product formation $\langle\tau_{off}\rangle^{-1}$ for mechanism B was about 6 times higher than that of mechanism A (Figure S22). In other words, this indicates that mechanism B produces resorufin molecules faster than mechanism A and that more resorufin molecules are produced in a certain time under mechanism B. This could be ascribed to the formation of more active and long-lived photocarriers primarily in CdS nanorod under mechanism B at both 405 and 532 nm.[56] In addition, we found two distinct dissociation kinetics in Au-tipped CdS heterostructures for both mechanisms A and B (Figure S23). The averaged rate of product dissociation $\langle\tau_{on}\rangle^{-1}$ for the e^- reactive sites in mechanism A was 1.46 s^{-1}, while $\langle\tau_{on}\rangle^{-1}$ in mechanism B it was 1.57 s^{-1}. The averaged rate of dissociation $\langle\tau_{on}\rangle^{-1}$ for the h^+ reactive sites in mechanism A was 0.41 s^{-1}, while $\langle\tau_{on}\rangle^{-1}$ in mechanism B it was 0.32 s^{-1}.

There is an important point that needs to be further discussed in Figure 6. Recently, Majima et al. proposed mechanism A in Au–TiO_2 hybrid particles to explain their finding from visible-light-induced redox reactions.[34] The results obtained here on the specifically designed Au-tipped CdS heterostructures directly verify the existence of two fundamentally distinct charge separation mechanisms together with the capability to optically control the direction of charge transfer on the heterostructures at the nanoscale.

Further Discussion on Photocatalytic Properties of Au–CdS Heterostructures. Besides the capability of tuning their photocatalytic selectivity, another advantage of hybrid metal–semiconductor heterostructures such as Au–CdS over its separate components is that we can control the photocatalytic activity by two methods. First, the photocatalytic activity in these hybrid heterostructures can be controlled by varying the metal (Au) loading on the semiconductor (CdS) nanorod under mechanism A at 532 nm. Specifically, we find that the rate of resorufin product formation rises fast when increasing the Au loading on the CdS nanorods at 532 nm (Figure S24). Mukherjee et al. have also demonstrated a steady increase of photocatalytic rate of HD molecule production with increasing Au loading on TiO_2.[41] Second, the photocatalytic activity can also be controlled by varying the wavelength of incident light, as supported by the spectra of Au–CdS hybrid heterostructures (Figure 1b, Figures S20 and S22). Therefore, it should be noted that Au–CdS hybrid heterostructures enable an efficient way to study and overcome important challenges in photocatalysis, such as providing synthetic and optical handles to control activity and perhaps, selectivity, in nanocatalysis.

The stability of Au–CdS heterostructures over our experimental time and conditions needs to be discussed. We recently demonstrated that metallic nanoparticles decorated on the CdS semiconductor surface significantly enhance activity and also greatly stabilize the CdS semiconductor nanorods against photoinduced degradation.[14] To clearly elucidate the stability of our Au–CdS heterostructures, we carried out ensemble measurements in the photocatalytic oxidation of amplex red to resorufin (see more details in the Supporting Information). We used a halogen lamp (150 W) to excite the Au–CdS heterostructures, and this lamp produces a continuous spectrum of light from 360 to 2000 nm. Therefore, under this illumination, both mechanisms are turned ON and operating in these heterostructures. We found that Au–CdS heterostructures are stable under our experimental conditions (Figures S25 and S26).

Because sunlight contains a wide range of wavelengths between the ultraviolet, visible and near-infrared spectral regions, we expect both mechanisms (A and B) to be active under direct sunlight illumination. Distinguishing between these two mechanisms and separating their individual contributions to overall photocatalytic activity (turnover) and selectivity is thus critical to fully understand, improve, and devise new solar-to-chemical energy conversion technologies. We expect these results will have an enormous positive impact in the development of better photocatalytic structures for solar-to-chemical energy conversion.

■ CONCLUSIONS

In conclusion, we report on the first direct measurements to resolve the nature and characteristic activities of two fundamental surface reactive sites (e^- and h^+) generated by photoinduced charge separation in single Au–CdS hybrid heterostructures during photocatalytic oxidations as models for other solar-to-chemical energy conversion reactions. Single-molecule photocatalysis with high-resolution superlocalization imaging allows us to reveal two distinct, incident energy-dependent charge separation mechanisms that result in completely opposite energy flows and polarities on single Au–CdS heterostructures. This finding is very important for the following reasons. First, it can help us design and develop better metal–semiconductor heterostructures that are highly

active for photocatalytic reactions under visible light. Second, it enables a better understanding of the nature and catalytic properties of single catalyst reactive sites in these heterostructures. Third, it permits us to potentially engineer the direction of energy flows on the heterostructured nanomaterials at the nanoscale. We therefore expect that our results have an enormous potential impact on the development of better photocatalyst structures.

EXPERIMENTAL SECTION

The Supporting Information contains more detailed experimental methods.

Single-Molecule Fluorescence Measurements. Single-molecule fluorescence experiments were carried out on a prism-type dual-color total internal reflection fluorescence (TIRF) microscope. A 532 nm laser beam (10 mW) was focused onto the sample to directly excite both Au−CdS hybrid heterostructures and the resorufin product molecules. Besides the 532 nm laser, a 405 nm laser beam (5 mW) was also used to excite the Au−CdS heterostructures in this study. The fluorescence from resorufin product during the oxidation reactions was collected via a Nikon Plan Fluor 100× oil iris objective (NA = 1.4) through a filter (532 LP, Chroma Technology Corp). All the fluorescence images were captured with an Andor iXonEM+ 897 CCD camera (Belfast, Northern Ireland). The collected movies and images were analyzed using MATLAB and NIH ImageJ (http://rsbweb.nih.gov/ij/). The fluorescence intensity trajectories were extracted from localized fluorescence spots individually across the entire movie. The intensity of each bright spot in an image was obtained by integrating the signal counts over an area of ∼1 μm^2.

ASSOCIATED CONTENT

Supporting Information

Experimental details, additional results and discussion, and supporting figures. This material is available free of charge via the Internet at http://pubs.acs.org.

AUTHOR INFORMATION

Corresponding Authors

nfang@iastate.edu
vela@iastate.edu

Notes

The authors declare no competing financial interest.

ACKNOWLEDGMENTS

This work was supported by the Laboratory Directed Research and Development Program of the Ames Laboratory, U.S. Department of Energy. The Ames Laboratory is operated for the U.S. Department of Energy by Iowa State University under contract no. DE-AC02-07CH11358.

REFERENCES

(1) Fujishima, A.; Honda, K. *Nature* **1972**, *238*, 37.
(2) Gratzel, M. *Nature* **2001**, *414*, 338.
(3) Cho, I. S.; Chen, Z.; Forman, A. J.; Kim, D. R.; Rao, P. M.; Jaramillo, T. F.; Zheng, X. *Nano Lett.* **2011**, *11*, 4978.
(4) Shankar, K.; Basham, J. I.; Allam, N. K.; Varghese, O. K.; Mor, G. K.; Feng, X.; Paulose, M.; Seabold, J. A.; Choi, K.-S.; Grimes, C. A. *J. Phys. Chem. C* **2009**, *113*, 6327.
(5) Walter, M. G.; Warren, E. L.; McKone, J. R.; Boettcher, S. W.; Mi, Q.; Santori, E. A.; Lewis, N. S. *Chem. Rev.* **2010**, *110*, 6446.
(6) Lewis, N. S. *Science* **2007**, *315*, 798.
(7) Sunada, K.; Kikuchi, Y.; Hashimoto, K.; Fujishima, A. *Environ. Sci. Technol.* **1998**, *32*, 726.
(8) Kumar, S.; Jones, M.; Lo, S. S.; Scholes, G. D. *Small* **2007**, *3*, 1633.
(9) Wu, K.; Zhu, H.; Liu, Z.; Rodriguez-Cordoba, W.; Lian, T. *J. Am. Chem. Soc.* **2012**, *134*, 10337.
(10) Bao, N. Z.; Shen, L. M.; Takata, T.; Lu, D. L.; Domen, K. *Chem. Lett.* **2006**, *35*, 318.
(11) Peng, X. G.; Manna, L.; Yang, W. D.; Wickham, J.; Scher, E.; Kadavanich, A.; Alivisatos, A. P. *Nature* **2000**, *404*, 59.
(12) Mokari, T.; Rothenberg, E.; Popov, I.; Costi, R.; Banin, U. *Science* **2004**, *304*, 1787.
(13) Alemseghed, M. G.; Ruberu, T. P. A.; Vela, J. *Chem. Mater.* **2011**, *23*, 3571.
(14) Ruberu, T. P. A.; Nelson, N. C.; Slowing, I. I.; Vela, J. *J. Phys. Chem. Lett.* **2012**, *3*, 2798.
(15) Berr, M.; Vaneski, A.; Susha, A. S.; Rodriguez-Fernandez, J.; Doblinger, M.; Jackel, F.; Rogach, A. L.; Feldmann, J. *App. Phys. Lett.* **2010**, *97*, 093108.
(16) Janet, C. M.; Viswanath, R. P. *Nanotechnology* **2006**, *17*, 5271.
(17) Menagen, G.; Macdonald, J. E.; Shemesh, Y.; Popov, I.; Banin, U. *J. Am. Chem. Soc.* **2009**, *131*, 17406.
(18) Amirav, L.; Alivisatos, A. P. *J. Phys. Chem. Lett.* **2010**, *1*, 1051.
(19) Dukovic, G.; Merkle, M. G.; Nelson, J. H.; Hughes, S. M.; Alivisatos, A. P. *Adv. Mater.* **2008**, *20*, 4306.
(20) Murdoch, M.; Waterhouse, G. I. N.; Nadeem, M. A.; Metson, J. B.; Keane, M. A.; Howe, R. F.; Llorca, J.; Idriss, H. *Nat. Chem.* **2011**, *3*, 489.
(21) Costi, R.; Saunders, A. E.; Elmalem, E.; Salant, A.; Banin, U. *Nano Lett.* **2008**, *8*, 637.
(22) Xiao, X.; Pan, S.; Jang, J. S.; Fan, F.-R. F.; Bard, A. J. *J. Phys. Chem. C* **2009**, *113*, 14978.
(23) Novo, C.; Funston, A. M.; Mulvaney, P. *Nat. Nanotechnol.* **2008**, *3*, 598.
(24) Tang, M. L.; Liu, N.; Dionne, J. A.; Alivisatos, A. P. *J. Am. Chem. Soc.* **2011**, *133*, 13220.
(25) Liu, N.; Tang, M. L.; Hentschel, M.; Giessen, H.; Alivisatos, A. P. *Nat. Mater.* **2011**, *10*, 631.
(26) De Cremer, G.; Sels, B. F.; De Vos, D. E.; Hofkens, J.; Roeffaers, M. B. J. *Chem. Soc. Rev.* **2010**, *39*, 4703.
(27) Chen, P.; Zhou, X.; Shen, H.; Andoy, N. M.; Choudhary, E.; Han, K.-S.; Liu, G.; Meng, W. *Chem. Soc. Rev.* **2010**, *39*, 4560.
(28) Tachikawa, T.; Majima, T. *Chem. Soc. Rev.* **2010**, *39*, 4802.
(29) Xu, W.; Kong, J. S.; Yeh, Y.-T.; Chen, P. *Nat. Mater.* **2008**, *7*, 992.
(30) Xu, W.; Kong, J. S.; Chen, P. *Phys. Chem. Chem. Phys.* **2009**, *11*, 2767.
(31) Xu, W.; Jain, P. K.; Beberwyck, B. J.; Alivisatos, A. P. *J. Am. Chem. Soc.* **2012**, *134*, 3946.
(32) Zhou, X.; Andoy, N. M.; Liu, G.; Choudhary, E.; Han, K.-S.; Shen, H.; Chen, P. *Nat. Nanotechnol.* **2012**, *7*, 237.
(33) Roeffaers, M. B. J.; Sels, B. F.; Uji-i, H.; De Schryver, F. C.; Jacobs, P. A.; De Vos, D. E.; Hofkens, J. *Nature* **2006**, *439*, 572.
(34) Tachikawa, T.; Yonezawa, T.; Majima, T. *ACS Nano* **2012**, *7*, 263.
(35) De Cremer, G.; Roeffaers, M. B. J.; Bartholomeeusen, E.; Lin, K.; Dedecker, P.; Pescarmona, P. P.; Jacobs, P. A.; De Vos, D. E.; Hofkens, J.; Sels, B. F. *Angew. Chem., Int. Ed.* **2010**, *49*, 908.
(36) Roeffaers, M. B. J.; De Cremer, G.; Libeert, J.; Ameloot, R.; Dedecker, P.; Bons, A.-J.; Bückins, M.; Martens, J. A.; Sels, B. F.; De Vos, D. E.; Hofkens, J. *Angew. Chem., Int. Ed.* **2009**, *48*, 9285.
(37) Shaviv, E.; Schubert, O.; Alves-Santos, M.; Goldoni, G.; Di Felice, R.; Vallée, F.; Del Fatti, N.; Banin, U.; Sönnichsen, C. *ACS Nano* **2011**, *5*, 4712.
(38) Robinson, R. D.; Sadtler, B.; Demchenko, D. O.; Erdonmez, C. K.; Wang, L.-W.; Alivisatos, A. P. *Science* **2007**, *317*, 355.
(39) Saunders, A. E.; Popov, I.; Banin, U. *J. Phys. Chem. B* **2006**, *110*, 25421.
(40) Mongin, D.; Shaviv, E.; Maioli, P.; Crut, A.; Banin, U.; Fatti, N. D.; Vallee, F. *ACS Nano* **2012**, *6*, 7034.
(41) Mukherjee, S.; Libisch, F.; Large, N.; Neumann, O.; Brown, L. V.; Cheng, J.; Lassiter, J. B.; Carter, E. A.; Nordlander, P.; Halas, N. J. *Nano Lett.* **2012**, *13*, 240.

(42) Moskovits, M. *Science* **2011**, *332*, 676.
(43) Anderson, P. A. *Phys. Rev.* **1959**, *115*, 553.
(44) Frischkorn, C.; Wolf, M. *Chem. Rev.* **2006**, *106*, 4207.
(45) Christopher, P.; Xin, H.; Linic, S. *Nat. Chem.* **2011**, *3*, 467.
(46) Mubeen, S.; Lee, J.; Singh, N.; Kramer, S.; Stucky, G. D.; Moskovits, M. *Nat. Nanotechnol.* **2013**, *8*, 247.
(47) Mubeen, S.; Hernandez-Sosa, G.; Moses, D.; Lee, J.; Moskovits, M. *Nano Lett.* **2011**, *11*, 5548.
(48) Lee, J.; Mubeen, S.; Ji, X.; Stucky, G. D.; Moskovits, M. *Nano Lett.* **2012**, *12*, 5014.
(49) Jakob, M.; Levanon, H.; Kamat, P. V. *Nano Lett.* **2003**, *3*, 353.
(50) Ruberu, T. P. A.; Vela, J. *ACS Nano* **2011**, *5*, 5775.
(51) Ishibashi, K.-I.; Fujishima, A.; Watanabe, T.; Hashimoto, K. *J. Phys. Chem. B* **2000**, *104*, 4934.
(52) Hoffmann, M. R.; Martin, S. T.; Choi, W.; Bahnemann, D. W. *Chem. Rev.* **1995**, *95*, 69.
(53) Thompson, T. L.; Yates, J. T. *Chem. Rev.* **2006**, *106*, 4428.
(54) Chih, T.; Jao, H.-J.; Wang, C. M. *J. Electroanal. Chem.* **2005**, *581*, 159.
(55) Gorris, H. H.; Walt, D. R. *J. Am. Chem. Soc.* **2009**, *131*, 6277.
(56) Wu, K.; Rodríguez-Córdoba, W. E.; Yang, Y.; Lian, T. *Nano Lett.* **2013**, *13*, 5255.
(57) Fujishima, A.; Zhang, X.; Tryk, D. A. *Surf. Sci. Rep.* **2008**, *63*, 515.
(58) Chong, R.; Rho, J.-E. R.; Yoon, H. J.; Rho, T.-H. D.; Park, P. S.; Kim, Y.-H.; Lee, J. H. *Biosens. Bioelectron.* **2012**, *32*, 19.
(59) Chong, R.; Rho, J.-E. R.; Yoon, H.-J.; Park, P. S.; Rho, T.-H. D.; Park, J. Y.; Park, L.; Kim, Y.-H.; Lee, J. H. *Talanta* **2013**, *116*, 403.
(60) Thetford, A.; Hutchings, G. J.; Taylor, S. H.; Willock, D. J. *Proc. Roy. Soc. A* **2011**, *467*, 1885.
(61) Baptista, L.; Clemente da Silva, E.; Arbilla, G. *Phys. Chem. Chem. Phys.* **2008**, *10*, 6867.
(62) Popham, P.; Novacky, A. *Plant Physiol.* **1991**, *96*, 1157.
(63) Giovanelli, D.; Lawrence, N. S.; Jiang, L.; Jones, T. G. J.; Compton, R. G. *Sens. Actuators, B* **2003**, *88*, 320.
(64) Lawrence, N. S.; Davis, J.; Jiang, L.; Jones, T. G. J.; Davis, S. N.; Compton, R. G. *Analyst* **2000**, *125*, 661.
(65) Costentin, C.; Robert, M.; Savéant, J.-M. *J. Am. Chem. Soc.* **2006**, *128*, 8726.
(66) Burkitbaev, M. *High Energy Chem.* **2003**, *37*, 216.
(67) Tiee, J. J.; Wampler, F. B.; Oldenborg, R. C.; Rice, W. W. *Chem. Phys. Lett.* **1981**, *82*, 80.
(68) Fang, H.-J.; Dong, W.-B.; Zhang, R.-X.; Hou, H.-Q. *Acta Phys. Chim. Sin.* **2006**, *22*, 761.